*Progress In Electromagnetics Research C, Vol. 110, 267–283, 2021*

# The Performance of Circularly Polarized Phased Sub-Array Antennas for 5G Laptop Devices Investigating the Radiation Effects

**Korany R. Mahmoud[1, 2, *], Abdullah Baz[3], Wajdi Alhakami[4], Hosam Alhakami[5], and Ahmed M. Montaser[6]**

**Abstract**—In this paper, the performance of circularly polarized (CP) adaptive sub-arrays integrated into 5G laptop device is investigated in the presence of a whole-body human phantom model. In addition, the radiation effect of the steered beam patterns has been analyzed by calculating the specific absorption rate distribution and temperature rise. In this target, a single-feed CP antenna element has been firstly designed to resonate at 28 GHz with high realized gain and radiation efficiency. Then, 4 sub-arrays have been constructed in a rectangular configuration with four-elements for each sub-array. To let the study more realistic, a complete human model is considered to investigate the radiation effects. The measured reflection coefficient and realized gain results of the designed antenna element are found to be −30 dB and 7.82 dB, respectively, in the assigned frequency band. Likewise, the antennas sub-arrays have approximately kept the same impedance matching attitude with high insertion loss of −22 dB and a realized gain and radiation efficiency of 16.85 dB and 86%, respectively, on average. Furthermore, the sub-arrays scan patterns and coverage efficiency have been studied considering the existence of the human body in different scenarios. Regarding the RF exposure, the results show that the resultant maximum values of specific absorption rate and power density do not exceed 1.52 W/kg and 3.5 W/m$^2$, respectively, whereas the maximum exposure temperature in such a case is less than 2.8°C after 30 minutes and decreases to 0.5°C after a penetration depth of 3 mm which reflects the possibility of safe use.

## 1. INTRODUCTION

Nowadays, commercial fifth generation (5G) services are already here, and the coming years will see more launches all over the world. 5G will significantly impact the tech industry, and it will definitely bring more value to consumers [1]. In general, 5G provides the broadband connection with a super low latency and also with very broad coverage, which means that it can support more devices such as a laptop to always connect to the internet, to the cloud, with a similar user experience as their mobile phone with 5G. Recently, different designs of 5G laptops have been announced such as Dell's Latitude 9510, HP's Elite Dragonfly G2, and the Lenovo Yoga 5G [2–4]. Two of those laptops (the Dragonfly and the Latitude) are business-focused devices that are not really aimed at consumers, and both only offer 5G as a configurable option, not as the default. However, the Lenovo Yoga 5G has some interesting features. Specifically, it packs nine antennas for stronger 5G signals and will support both sub-6 GHz and millimeter wave (mm-wave) technologies that are crucial to the network.

*Received 20 January 2021, Accepted 10 March 2021, Scheduled 12 March 2021*

* Corresponding author: Korany Ragab Mahmoud (kurany_hameda@h-eng.helwan.edu.eg).

[1] Department of Electronics and Communications, Faculty of Engineering, Helwan University, Cairo, Egypt. [2] National Telecommunications Regulatory Authority, Ministry of Communication and Information Technology, Giza, Egypt. [3] Computer Engineering Department, College of Computer and Information Systems, Umm Al-Qura University, Makkah, Saudi Arabia. [4] Department of Computer Science, College of Computer and Information Technology, Taif University, P. O. Box 11099, Taif 21944, Saudi Arabia. [5] Department of Computer Science, College of Computer and Information Techonogy, Umm Al-Qura University, Makkah 21955, Saudi Arabia. [6] Electrical Engineering Department, Sohag University, Sohag, Egypt.

In the world radio-communication conference 2019 (WRC-19), the delegates have recognized additional radio-frequency bands, which will facilitate the development of 5G cellular networks [5], whereas the frequency bands of 24.25–27.5 GHz, 37–43.5 GHz, 45.5–47 GHz, 47.2–48.2 GHz, and 66–71 GHz have been identified. However, these high frequencies experience more sensitivity to blockages and large path loss. Therefore, the use of an antenna array becomes a necessity to steer directional beam patterns consistent to high gain for multi-gigabit per second data rates [6]. Furthermore, an imperative need appears to realize circular polarization (CP) phased array antennas to enhance the efficiency of mm-wave reception and transmission [7, 8].

Generally, CP can be achieved using various feed arrangements or slight modifications made to the elements [9]. In [10], two orthogonal modes are excited with a 90° time-phase difference to circularize the antenna polarization. On the other hand, the use of a thick superstrate above the radiator with an air gap (Fabry-Perot cavity antennas) can be used to increase the gain and improve the axial ratio (AR) significantly [11]; however, these designs possess poor mechanical properties due to the presence of air gap and have high profiles. The antennas with multiple stacked substrates without air gap can also be used for CP radiations [12] but have the drawbacks of complex design and high structures thickness. On the other hand, metasurfaces are combined with radiators to achieve wideband AR and gain enhancement [13]. These configurations have design complexities, high-profiles, and poor mechanical properties because of the air gap. In [14], a single-feed broadband circularly polarized microstrip antenna operating in millimeter-wave band at 28 GHz is designed with the AR and antenna gain of −17 dB and 6.49 dBi, respectively. Recently, many designs of dual-polarized mm-wave base stations have been introduced for 5G communication systems [15]. In 2017, the world's first reported Si mm-wave phased array antenna module of 64 dual-polarized antennas has been reported by IBM and Ericsson announced operating at 28 GHz [16].

Nevertheless, an innovative design of laptops with beam-steering capabilities is essentially needed for 5G networks. To the best of our knowledge, there have been no systematic researches undertaken so far concerning beam steering of 5G mm-wave laptop devices. Thus, in this paper, a design of a single-feed CP antenna element implemented into a single substrate is firstly introduced and verified at the operating frequency of 28 GHz. Then, 4 sub-arrays in a rectangular arrangement are embedded into the laptop base to steer the beam patterns by optimizing the excitation phases, whereas the effects of the laptop structure and whole-body phantom model on the beam steering capability will be involved. In this regard, the modified version of hybrid gravitational search algorithm and particle swarm optimization (MGSA-PSO) have been utilized to optimize the antenna dimensions and also the sub-arrays feeding phases [17]. The designed sub-arrays and optimization algorithm can be generalized to steer the beam-pattern for numerous scenarios. However, in this paper, only four different scenarios have been presented to prove the capability of the introduced design as possible candidates for future mm-wave 5G laptop devices.

On the other hand, the absorption amount of electromagnetic (EM) energy in human tissues from radio frequency (RF) devices and systems plays a vital role in the system applicability [18–26]. Therefore, precautions should be taken into account in the form and distribution of antennas within modern wireless communication devices that are provided to end users. Therefore, safety standards and guidelines have been organized, identified, and implemented to protect human bodies from exposure to radiation emitted by these devices. In the latest revisions of both IEEE and ICNIRP standard/guideline [27, 28], the reference levels of incident power density for local exposure over 6 GHz are proposed to be frequency-dependent values of $275 f_{\mathrm{GHz}}^{-0.177}$ and $55 f_{\mathrm{GHz}}^{-0.177}$ for occupational exposure/restricted environment and general public exposure/unrestricted environment, respectively. The incident power density is averaged over 6 min for local exposure over any 4 $\mathrm{cm}^2$ of body surface and allows to exceed by a factor of 2, with an averaging area of 1 $\mathrm{cm}^2$. For occupational exposures, the limits for local exposure are intended to limit skin temperature increases in a continually exposed person to about 2–3°C. However, evaluations based on power density (PD) depend only on the density of power traveling toward the tissues and do not rely on knowledge of the distribution of fields or power absorption in the tissues, unlike evaluations of specific absorption rate (SAR) or temperature [29]. Hence, PD is not as useful as SAR or temperature for evaluating safety in mm-wave devices, especially in the near field. Therefore, SAR has been used in several studies as one of the dosimetric quantities at mm-waves to study the exposure [29–34]. Therefore, it is important to conclude the temperature elevation in

the human tissues along with SAR and/or PD values calculations, whereas the rise in temperatures in human tissues after exposure to radiation indicates high power absorbed in these tissues [35]. Therefore, in this paper, both SAR distribution and temperature rise in biological tissues from the mm-wave 5G laptop in different scenarios have been investigated, in addition to the PD evaluation for the worst case scenario.

The presented paper is organized as follows. In Section 2, the design configuration of CP antenna element and sub-arrays integrated into the laptop device are introduced. The results are presented and discussed in Section 3. Finally, Section 4 concludes the results.

## 2. DESIGNS AND CONFIGURATIONS

This section presents firstly the design structure of the proposed CP antenna element. Then, the geometrical arrangement of the suggested 4 sub-arrays is introduced, and each sub-array consists of 4 antenna elements. The sub-arrays are then integrated inside a laptop in order to consider its structure effect on the radiation characteristics. Furthermore, a whole-body human model is involved to investigate the radiation effects.

### 2.1. Configuration of Antenna Element Design

The proposed antenna is designed through many stages of development, until it reaches its final shape, which realizes the required radiation characteristics such as reflection coefficient ($S_{11}$), gain, radiation efficiency ($e$), and AR. The 3D structure designs of different stages are presented in Figs. 1(a)–(e), and the antennas are fed by a microstrip line. In the beginning, a simple antenna with a printed radiated patch in binomial-curved shape and partial ground plane in the bottom layer is considered, named Ant. #1 as shown in Fig. 1(a). To circularize the antenna polarization, a pair of notches with a big cross slot is etched in the middle of the patch consisting of a horizontal slot with edges shaped like an anchor, while the vertical slot has flat edges, as shown in Fig. 1(b) for Ant. #2. In Ant. #3, the partial ground plane is modified with zigzag terminal shape as declared in Fig. 1(c) to improve the impedance matching [36]. Furthermore, two slots of L shape opposite to the right and left of the feed line are considered in Ant. #4 to improve the antenna gain [37]. Finally, fractal cross slots are etched on the patch as illustrated in Fig. 1(e) to enhance the antenna efficiency and polarization.

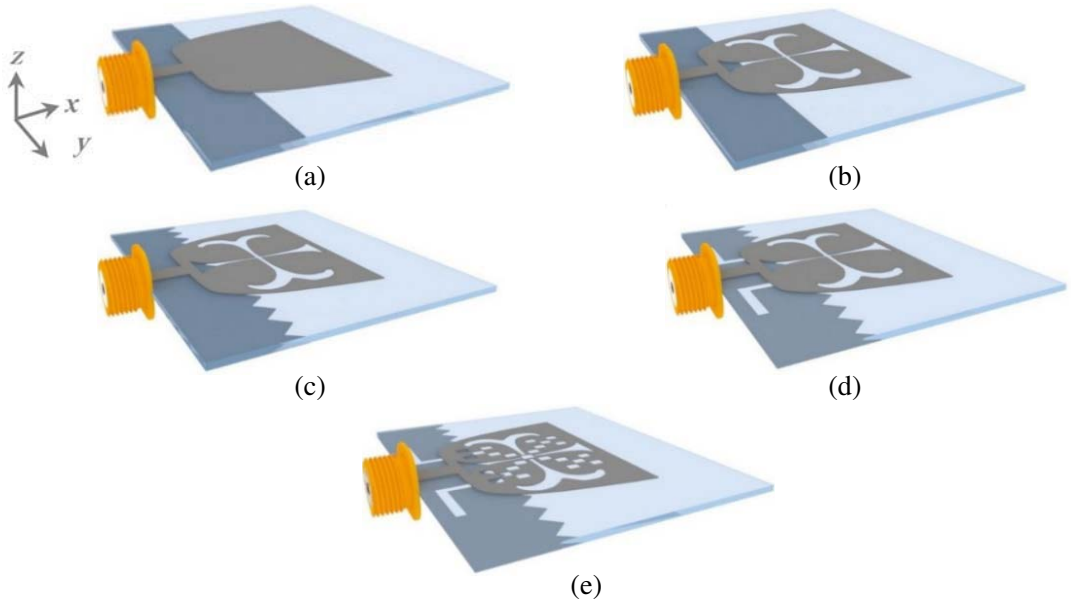


**Figure 1.** 3D metal pattern configuration of design strategies, (a) Ant. #1, (b) Ant. #2, (c) Ant. #3, (d) Ant. #4, and (e) final design.

The antenna structure is fabricated on a Rogers® Duroid™ RT5880 substrate of thickness and relative permittivity of 0.508 mm and $\varepsilon_{r_1} = 2.2$, respectively, and loss tangent $\tan\delta = 0.0009$ with overall dimension of $23.63 \times 30$ mm. The outer limits of the binomial patch are represented as $L_1 \times W_1$. Fig. 2 shows the top and back views of the proposed antenna illustrating the antenna dimensions. Generally, a symmetrical structure of the antenna is taken into consideration to make the radiation characteristics relatively stable almost over the entire bandwidth.

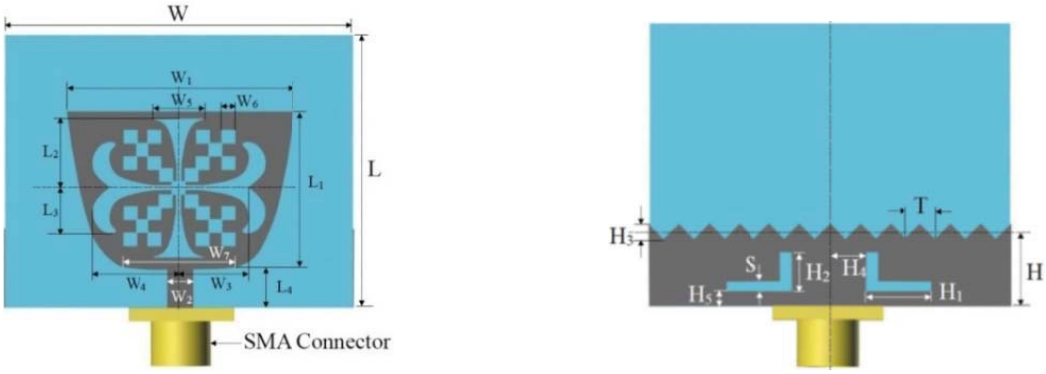


(a) (b)

**Figure 2.** Configuration of the CP mm-wave antenna, (a) front view, and (b) back view.

### 2.2. Antenna Array Design for mm-Wave 5G Laptop Devices

Figure 3 presents the geometrical configuration of the proposed sub-arrays based on the designed antenna element. The structure contains four sub-arrays; each one includes four antenna elements with center-to-center distance of approximately $4.65\lambda$. In the partial ground plane, a horizontal eight figure is etched between each two antenna elements as shown in the inserted figure to minimize the mutual coupling, increase the sub-array antenna gain, and reduce the grating lobes. In order to simulate reality, a generic laptop device is modeled as shown in Fig. 4. The overall dimensions of the laptop structure are: base unit ($22.7 \times 33 \times 2.4\,\text{cm}^3$) and screen ($22.7 \times 33 \times 0.5\,\text{cm}^3$) with an open angle ($\alpha$) = 95°. To mimic the laptop's internal shielding, a Lucite (dielectric plastic material) of relative permittivity $\varepsilon_{r_2} = 4.5$ and conductivity $\delta = 0.0004\,\text{S/m}$ is considered. As depicted in the figure, the configuration of the proposed sub-arrays is embedded into the base of a realistic laptop device.

To investigate the human body effects on the laptop beamforming capability and also to evaluate the whole-body area SAR and temperature rise, a well-known virtual tester model called Duke is involved in the simulation model. This numerical phantom is one from the virtual family available through the IT'IS Foundation [38], which has contributed significantly to the wealth of scientific knowledge on electromagnetic field health effects. Duke is 34-years old, 1.77 m tall, and weighs 70.2 kg. The anatomically realistic 3D-phantom is derived from magnetic resonance imaging scans of human subjects. The phantom is segmented into a number of tissue types and organs more than 300 in the whole-body model with a resolution of 0.5 mm, where each tissue type is assigned by suitable thermal and dielectric properties.

## 3. RESULTS AND DISCUSSIONS

In the beginning, the measured and simulated results of the optimized CP antenna element will be presented, analyzed, and compared as the building block of mm-wave array for 5G laptop devices. Then, the sub-arrays simulation results will be offered to show their capabilities for steering the beam patterns in the azimuth and oblique directions. Moreover, the laptop radiation effects on the human body will be analyzed by calculating the corresponding SAR distribution and temperature rise caused by each scenario.

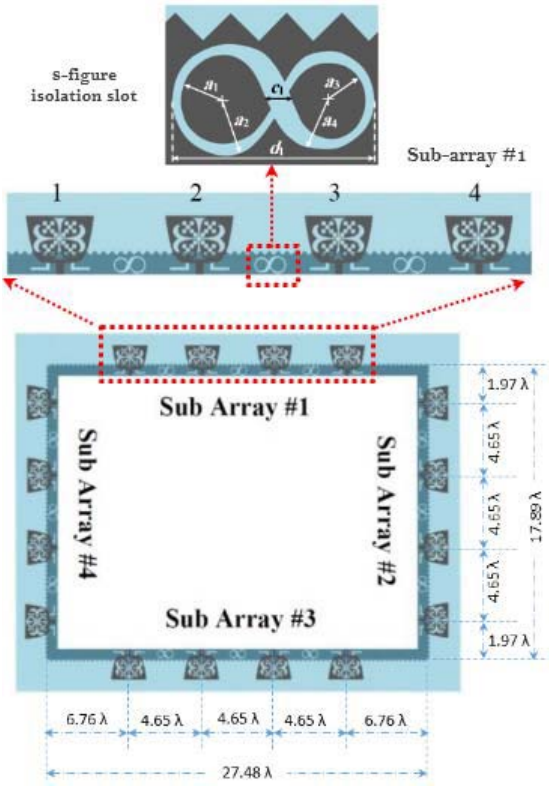


**Figure 3.** Configuration of the proposed antenna sub-arrays, the inset figure refers to the sub-array structure and the eight of figure isolation slot in ground plane.

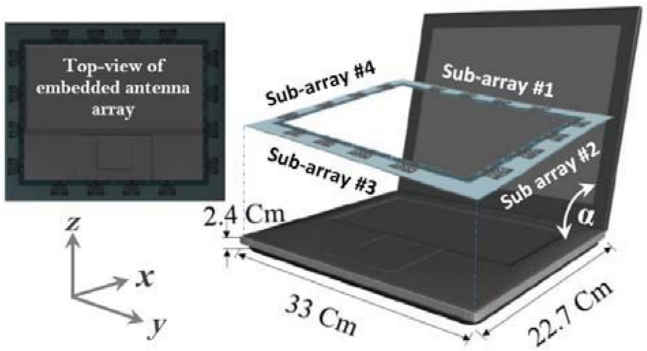


**Figure 4.** Configuration of the proposed antenna array embedded into realistic laptop.

### 3.1. Single Element Performance

The dimensions of the binomial patch and partial ground plane of the proposed antenna were optimized by the MGSA-PSO algorithm to resonate the antenna at 28 GHz with high gain, efficiency, and an AR less than 3 dB. The antenna is completely modeled using CST-MWS [39] which is linked with the optimization algorithm, MATLAB-coded, to optimize the antenna dimensions. To validate the results, the optimized antenna will also be modeled based on the finite difference time domain (FDTD) computational method through MATLAB code. In such a case, the following objective function is considered to maximize the antenna gain ($G$) and radiation efficiency ($e$) in addition to minimizing both return loss ($S_{11}$) and AR at the operating frequency band.

$$\text{Obj}_1 = [\min\{S_{11}(f) + \text{AR}(f)\} + \max\{G(f) + e(f)\}]_{f=28\,\text{GHz}} \quad (1)$$

By optimizing the antenna dimensions, a CP antenna matched at 28 GHz with acceptable gain and high efficiency can be obtained. Table 1 lists the variables' decision space and the best obtained values of the optimized antenna dimensions.

**Table 1.** The value of optimized dimensions (in millimeter).

| Variable | Initial value | Decision space | | Best value |
|---|---|---|---|---|
| | | from | to | |
| $W_1$ | 25 | 11 | 29.6 | 20.04 |
| $W_2$ | 1.75 | 1.4 | 2.5 | 2.11 |
| $W_3$ | 5 | $W_1/2-9$ | $W_1/2-3$ | 6.02 |
| $W_4$ | 6.2 | $W_1/2-10.5$ | $W_1/2-4.5$ | 7.51 |
| $W_5$ | 10 | 3 | $W_1-6.4$ | 4.75 |
| $W_6$ | 0.8 | 0.75 | 1.2 | 1.15 |
| $W_7$ | 12 | $W_2$ | $W_1+W_2-10$ | 9.95 |
| $W$ | – | – | – | 30 |
| $L_1$ | 12 | 11 | 15 | 13.55 |
| $L_2$ | 5 | $L_1/2-5$ | $L_1/2-0.5$ | 6.03 |
| $L_3$ | 3 | 2 | 6 | 4.02 |
| $L_4$ | 2.5 | 2 | 5.5 | 3.65 |
| $L$ | – | – | – | 23.63 |
| $H$ | 10 | 5 | 12 | 6.13 |
| $H_1$ | 3 | 1 | $W/2$ | 5.74 |
| $H_2$ | 2.5 | $H_5$ | $H-H_3/2$ | 3.42 |
| $H_3$ | 5 | 1 | 10 | 1.47 |
| $H_4$ | 4 | 1 | $W/2-H_1$ | 3.01 |
| $H_5$ | 1 | 1 | $H-H_3/2-H_2$ | 1.35 |
| $S$ | 0.5 | 0.25 | $H_2$ | 0.98 |
| $T$ | 3 | 2 | 6 | 2.51 |
| $d_1$ | 9 | 9 | 14 | 9.25 |
| $a_1$ | 1.7 | 1.5 | 2.5 | 1.95 |
| $a_2$ | 2 | $a_1+0.3$ | 3 | 2.38 |
| $a_3$ | 1.55 | 1.5 | 2.5 | 1.75 |
| $a_4$ | 1.7 | $a_3+0.2$ | 3 | 2.05 |
| $c_1$ | 1.2 | 1 | 2 | 1.25 |

Figure 5 illustrates the radiation characteristics for each stage. It can be observed that the impedance of target band is hardly matched in Ant. #1 with low gain and efficiency. In addition, the AR is found more than 7 dB. For Ant. #2, the AR at the center frequency of 28 GHz is decreased to 3 dB as depicted in Fig. 5(b). However, in Ant. #3, the impedance matching is improved as shown in Fig. 5(a) due to increasing the current path at the ground plane. Fig. 5(c) declares the enhancement in the antenna gain due to etched slots into the ground plane. Finally, the effects of fractal cross slots etched on the patch on the antenna polarization and efficiency are illustrated in Figs. 5(b) and 5(e), respectively.

To illustrate the effect of slots etched on the top and bottom layers of the optimized antenna, the instantaneous $E$-field in a longitudinal cut is represented in Fig. 6. It is observed that an omnidirectional field distribution is obtained in Ant. #1 as shown in Fig. 6(a), while the $E$-field is increased in the end-

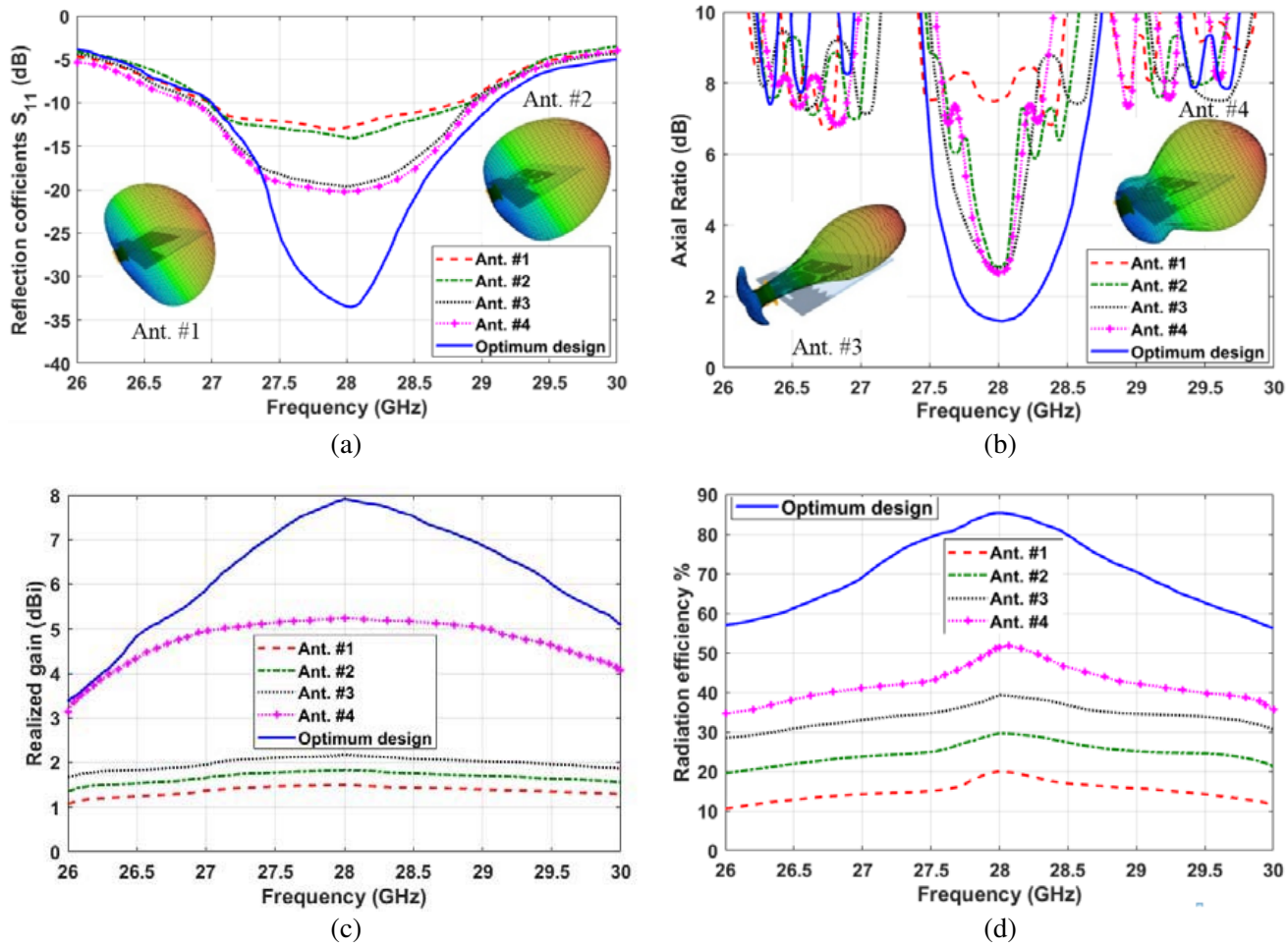


**Figure 5.** Comparison of the simulated results of different antenna stages using CST package, (a) return loss, (b) axial ratio, (c) gain, and (d) radiation efficiency. The inset figures illustrate the 3D radiation patterns.

fire direction $+x$ as shown in Fig. 6(b), whereas the wave-front is more directive than the case with no slots. In such a case, the surface wave above the optimized antenna radiates the energy to free space with a suitable phase constant to realize a stable end-fire radiation pattern.

Figure 7 illustrates the surface current distribution over the designed antenna at the operating frequency of 28 GHz. The simulated excited surface current is found to be balance and approximately symmetric about the longitudinal mid-antenna. As anticipated, the induced current density is increased along the feeder and most metallic parties of radiated patch specially on the patch perimeter as shown in Fig. 7(a). Thus, the current density along the antenna patch edges has a great influence on the antenna bandwidth enhancement. As illustrated in Fig. 7(b), the current flowed through the zigzag terminal shape in the ground plane which hence increased the electrical length.

To validate the simulated results, Figs. 8(a) and 8(b) present the measurements of the antenna reflection coefficient ($S_{11}$) and realized gain ($G$), respectively, compared with the results produced using the FDTD method and CST-MWS. It is noted that the obtained experimental and simulated results are in good agreement. The slight differences between them are related mainly to the manufacturing tolerances and antenna assembly inaccuracy. Photographs of the front and back views of the fabricated antenna are inserted in Figs. 8(a) and 8(b), respectively. As illustrated in the figures, the designed antenna has achieved good matching impedance and high realized gain at the operating frequency with measured values of $S_{11} < -33.46$ dB and $G = 7.93$ dBi, respectively. This performance is achieved as an effect of well-designed radiator patch binomial shape and etched fractal slots which are also responsible

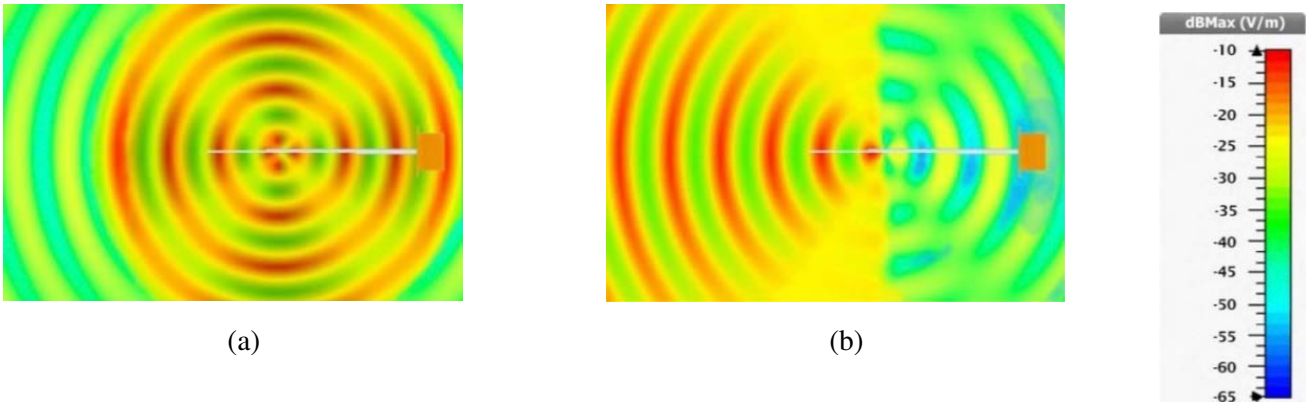


**Figure 6.** The instantaneous $E$-field in a longitudinal cut, (a) Ant. #1 without any slots and (b) optimized antenna.

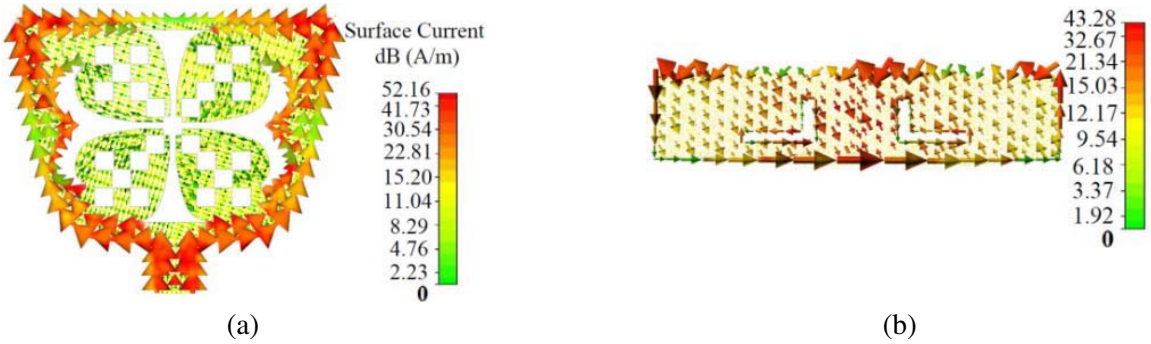


**Figure 7.** Simulated current distribution of the optimized mm-wave antenna, (a) through the patch and (b) through the ground plane.

for increasing the radiation efficiency up to 86% as shown in Fig. 8(c). On the other side, the main cross slot in middle of binomial patch greatly improves the AR due to collecting the current around their edges. The simulated results of AR is found to be less than 3 dB from 27.65 to 28.41 GHz as depicted in Fig. 8(d). Fig. 9 shows the simulated and measured 2D radiation patterns of the designed antenna at 28 GHz. As shown, good agreement is observed between simulated and measured results in $E$ and $H$-planes.

### 3.2. Performance of Antenna Sub-Arrays Embedded into 5G Laptop Device

Firstly, the sub-array antenna elements are excited with the same amplitudes and phases of (1, 0°) to investigate the mutual coupling effect between the antenna elements. The sub-array is simulated also with FDTD MATLAB code to compare the results with those obtained using CST package to validate the results. Fig. 10 illustrates the results agreement for sub-array characteristics such as $S$-parameters, antenna gain, and radiation efficiency. The sub-array $S$-parameters results in the case of uniform feeding are illustrated in Fig. 10(a). It is obvious that the sub-array antennas have a good reflection coefficient of $-30$ dB at the resonance frequency with weak mutual coupling between sub-array elements getting below $-23$ dB. Furthermore, an acceptable realized gain of 14.8 dBi is obtained at operating frequency of 28 GHz as depicted in Fig. 10(b) with a radiation efficiency of 79.12%.

Now, the beam steering capability of the 5G laptop device in the vicinity of whole-body human phantom model will be studied in azimuth and oblique directions. In this target, four scenarios will be investigated. Scenarios #1, #2, and #3 will be considered for azimuthal directions ($\theta = 90°$) at $\varphi = 0°$, 90° and 180°, respectively, while in scenario #4 the direction of the main beam-pattern is assumed

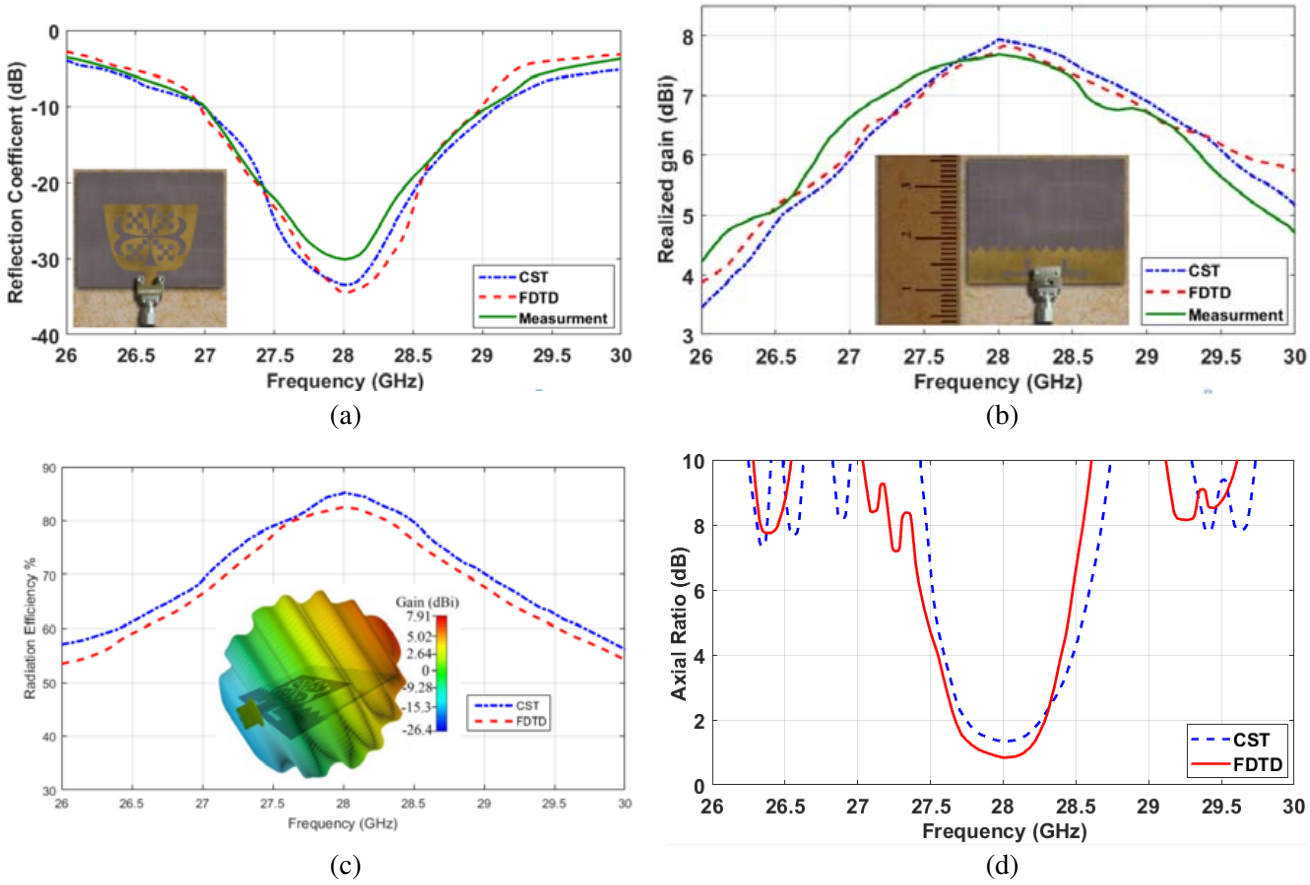


**Figure 8.** Measured and simulated radiation characteristics of the optimized antenna, (a) return loss, (b) gain, (c) radiation efficiency, and (d) axial ratio.

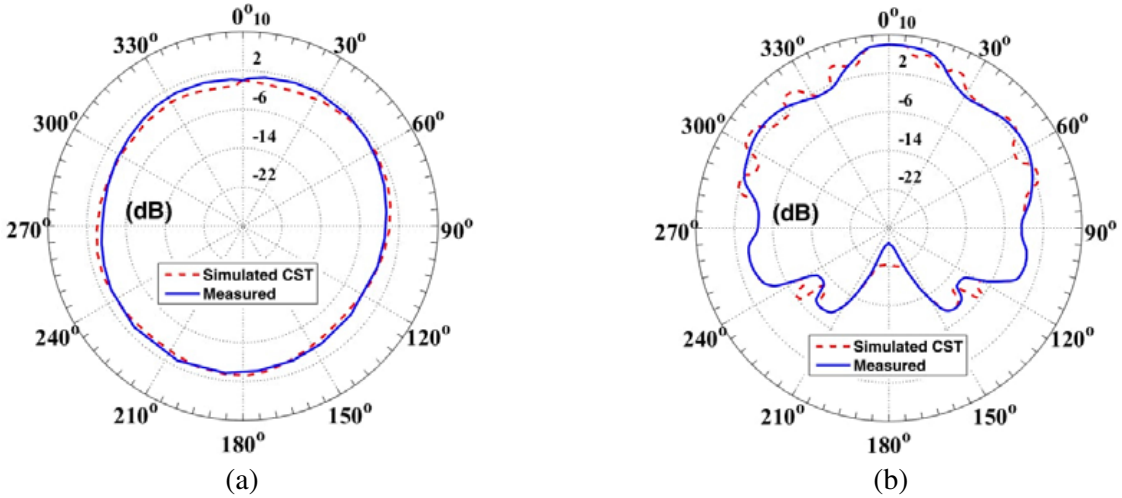


**Figure 9.** Measured and simulated 2D radiation patterns of the designed antenna at 28 GHz, (a) $y$-$z$ plane, and (b) $x$-$z$ plane.

to be at $(\theta, \varphi) = (45°, 315°)$. As a powerful optimization technique, the MGSA-PSO is considered to optimize the feeding phases of the corresponding sub-array antenna elements. To realize the beam-pattern direction for each scenario, the following objective function is applied to maximize the sub-array

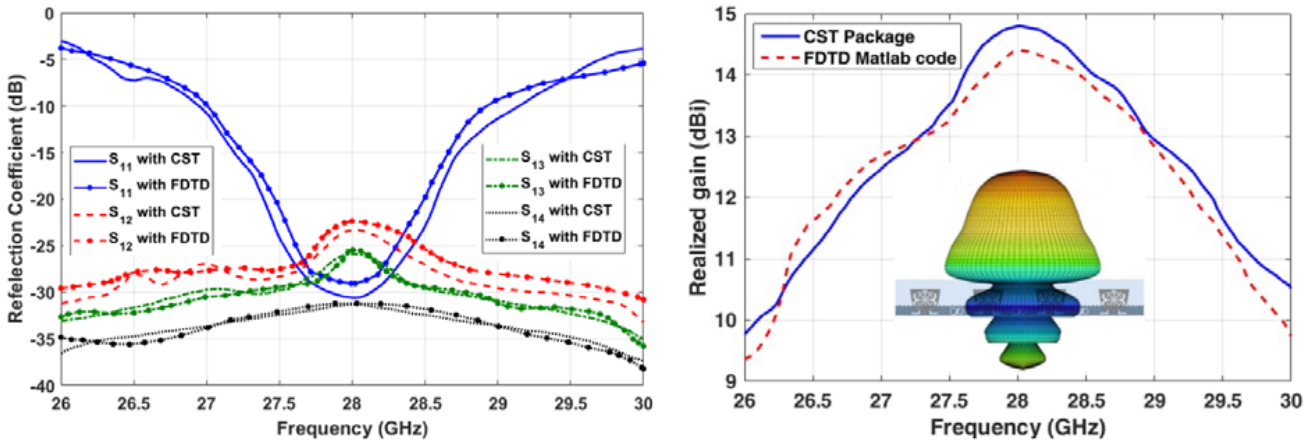


**Figure 10.** Simulated radiation characteristics of sub-array antenna elements, (a) $S$-parameters, (b) realized gain, and (c) radiation efficiency. The inset figure illustrates the 3D radiation patterns.

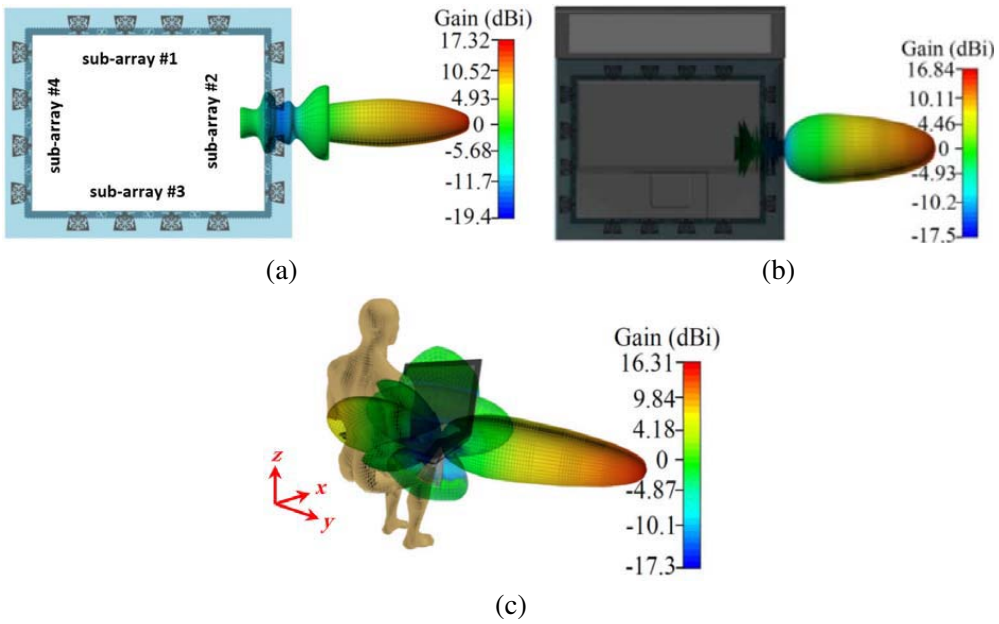


**Figure 11.** Simulated 3D gain patterns of the sub-array #2 to steer the beam-pattern at $\varphi = 90°$, (a) in free space, (b) embedded into laptop, and (c) in the presence of whole-body human model.

total field, $E_t(\theta_i, \varphi_i)$, toward the desired direction.

$$\text{Obj}_2 = \max |E_t(\theta_i, \varphi_i)| \tag{2}$$

For different scenarios, the phases of sub-array antenna elements were allowed to vary from $-\pi$ to $+\pi$. In the beginning, the capability of the embedded sub-arrays antennas into laptop device to synthesize the beam-pattern has been examined considering the presence of human body. Therefore, the feeding phases of sub-array #2 have been optimized to steer the beam-pattern at $\theta = \varphi = 90°$ (scenario #2) in the following three cases. In the first case, the sub-array is put stand-alone in free space without any casing, while in the second case the sub-array is embedded inside the laptop.

Finally, the existence of the whole-body human model in the simulation domain will be considered to estimate the whole effects on the laptop beam steering capability. Fig. 11(a) illustrates the optimized

beam pattern in the case of locating the sub-array in free space, whereas the calculated gain is found to be 17.32 dBi which is higher than the expected gain in an ideal condition (14.11 dBi) due to the effect of the eight-of-figure slots in the ground plane and optimizing the feeding phases. Fig. 11(b) shows the effect of the laptop structure on the radiation pattern. It can be observed that the realized gain is slightly decreased by 0.48 dBi with increase in the main-lobe beam-width. Fig. 11(c) illustrates the laptop device ability to steer the beam-pattern into the desired direction in the existence of a whole-body human model. It is well seen that the realized gain is decreased with only 0.53 dBi compared to case #2 which is more relevant to the generated side-lobes.

Similarly, the capability of the laptop device to steer the beam-patterns as proposed in scenarios #1, #3, and #4 is tested. As shown in Figs. 12(a) and 12(b), the feeding phases of sub-arrays #1 and #3 are optimized to steer the beam-patterns (perpendicular to the direction of the corresponding sub-array) at $\varphi = 0°$ and $\varphi = 180°$, respectively. The obtained results illustrate the capability of the device to steer the beam-pattern in the assigned directions effectively with an acceptable gain. However, for scenario #4, the complexity is increased, whereas the desired direction, which usually refers to the router location, is located at the vertical altitude of $\theta = 45°$ at $\varphi = 315°$. In such a case, using sub-array #4 only to steer the beam-pattern has shown partial inability to exactly maximize the field at this direction, in addition to generating many high amplitude side-lobes as shown in Fig. 12(c). Therefore, in this case sub-arrays #4 and #1 are collaborated to steer the beam-pattern as shown in Fig. 12(d). That is the main reason for the increased value of the realized gain to 24.51 dBi in this scenario, compared to 17.58 dBi, 16.31 dBi, and 16.26 dBi for scenarios #1, #2, and #3, respectively.

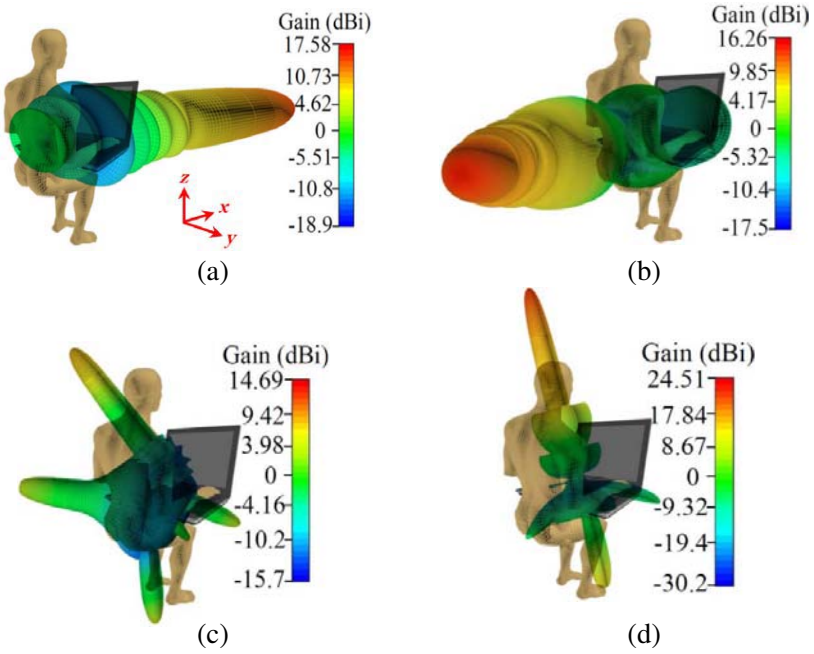


**Figure 12.** Optimized 3D beam patterns of the sub-arrays antenna package for different scenarios, (a) scenario #1, (b) scenario #3, (c) scenario #4 considering sub-array #4 and (d) scenario #4 considering sub-arrays #1 and #4.

Table 2 includes the respective phase for each antenna element that was optimized to achieve the desired radiation pattern in addition to the corresponding gain and side lobe level (SLL) for each scenario. It is clear that the SLL for scenario #4 considering sub-arrays #1 and #4 is decreased to −27.35 dB compared to −5.87 dB in the case of considering only sub-array #4. The acceptable SLLs of −19.56 dB, −24.16 dB, and −20.67 dB have been obtained for other scenarios #1, #2, and #3, respectively.

Figure 13 investigates the total scan pattern (TSP) of the presented scenarios. The TSP of each antenna sub-array is obtained by extracting the best achievable gain value at every angular distribution

**Table 2.** The optimized feeding phases for each scenario and corresponding results.

| Antenna element | Scenario #1 | Scenario #2 | Scenario #3 | Scenario #4 | Scenario #4 | |
|---|---|---|---|---|---|---|
| | Sub-array #1 | Sub-array #2 | Sub-array #3 | Sub-array #4 | Sub-array #1 | Sub-array #4 |
| No. 1 | −50.36° | 173.30° | −23.69° | 164.27° | −36.27° | 73.68° |
| No. 2 | 141.95° | −6.84° | 89.15° | −16.51° | 56.41° | −161.42° |
| No. 3 | 86.14° | −94.73° | 65.23° | −101.72° | 124.21° | 9.53° |
| No. 4 | −170.52° | −31.26° | −145.76° | 44.67° | −29.31° | −18.65° |
| SLL (dB) | −19.56 | −24.16 | −20.67 | −5.87 | −27.35 | |
| $G$ (dBi) | 17.58 | 16.31 | 16.26 | 14.69 | 24.51 | |

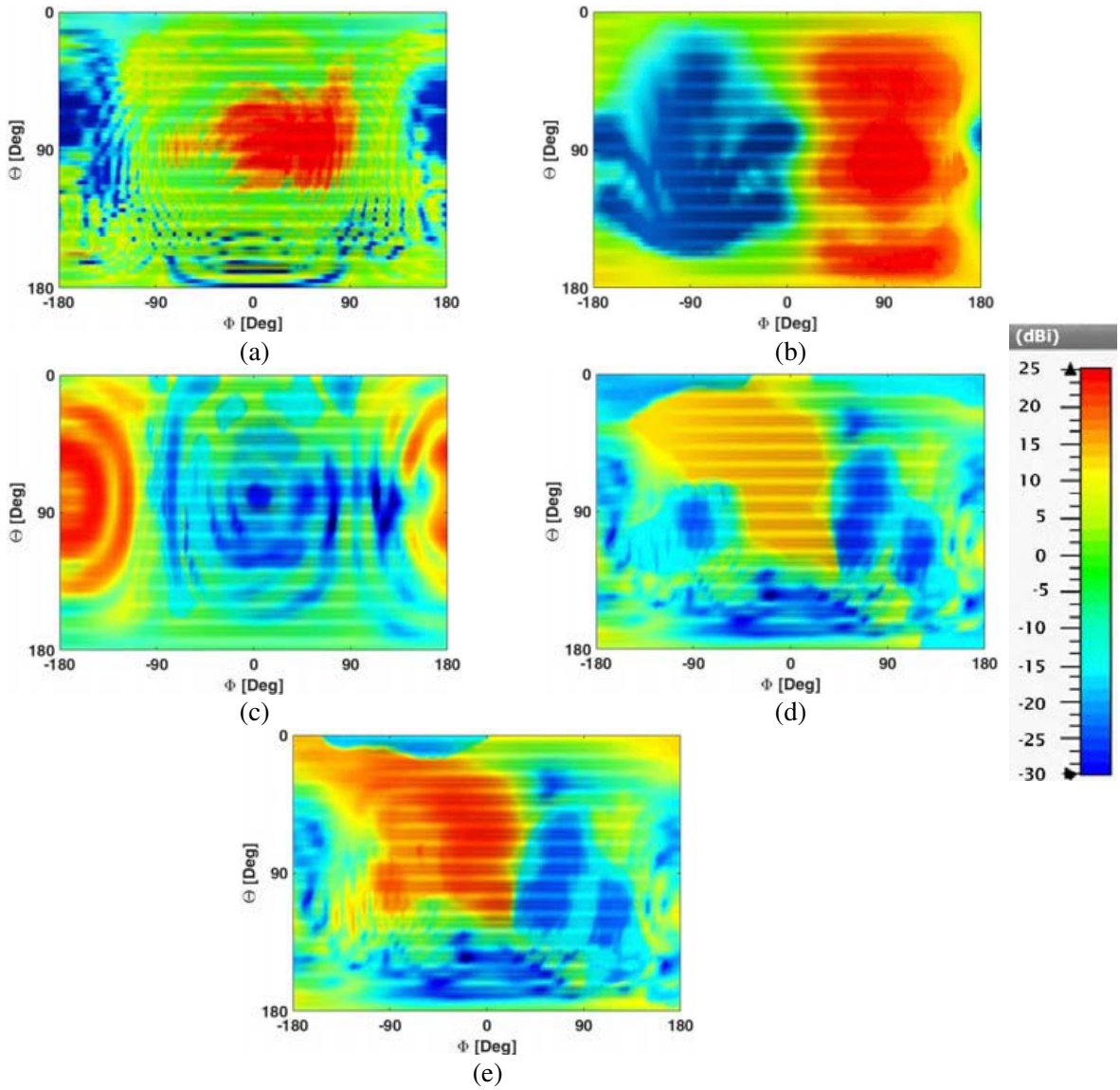


**Figure 13.** Total scan pattern for different scenarios, (a) scenario #1, (b) scenario #2, (c) scenario #3, (d) scenario #4 considering sub-array #4, (e) scenario #4 considering sub-arrays #1 and #4.

point. The choices of the element spacing and phase excitations ensure that each sub-array has sufficiently wide coverage. Figs. 13(a), 13(b), and 13(c) show that each sub-array can effectively converge its corresponding direction as required in scenarios #1, #2, and #3. However, for scenario #4, it is clear that better TSP performance can be obtained considering sub-arrays #1 and #4 than that achieved considering only sub-array #4 as illustrated in Figs. 13(d) and 13(e).

Furthermore, the consistent coverage efficiencies ($\eta_c$) as a function of minimum received gain ($G_{\min}$) are computed for the sub-arrays at different scenarios as illustrated in Fig. 14. It is clear that the coverage efficiency has dropped to 88.5% when the threshold gain exceeds 5 dBi for subarray #1 and reduced to 86.55%, 74.13%, and 77.8% for subarrays #2, #3, and #4, respectively. From the above, it is observed that subarray #3 has the lowest coverage efficiency which is related to the existing human body between the laptop and the desired location.

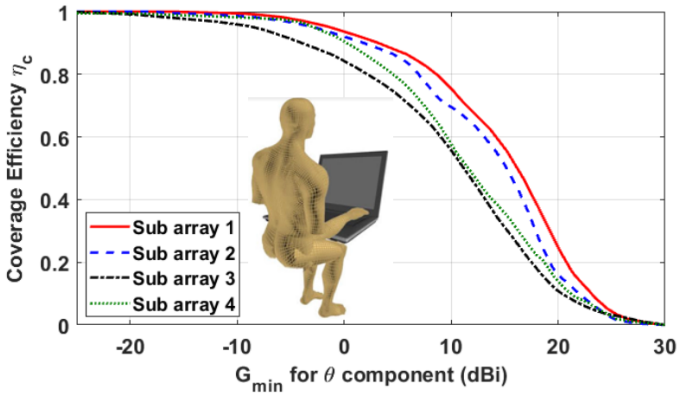


**Figure 14.** Coverage efficiency as a function of minimum received gain.

### 3.3. RF Exposure Results

Now, the radiation effects of the sub-arrays embedded into 5G laptop on the human body are investigated. Fig. 15 shows the SAR distribution in different scenarios. It is possible to clearly observe the effect of the RF electromagnetic field exposure on the whole-body human model for each scenario. It is noticeable that the worst case of peak SAR was recorded by the 3rd scenario whereas the beam directly penetrates the human body. However, it should be noted that the resultant peak value of SAR does not exceed 1.52 W/kg as obtained in scenario #3, but on the contrary, it is decreased to 0.54 W/kg for the 1st scenario.

The PD calculations for the worst case (Scenario #3) in the $-x$ direction is presented in Fig. 16.

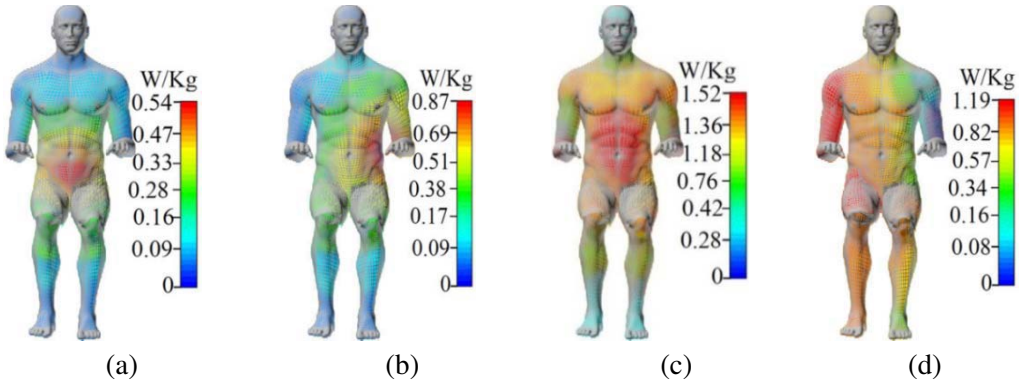


**Figure 15.** SAR distribution for different scenarios, (a) scenario #1, (b) scenario #2, (c) scenario #3 and (d) scenario #4 utilizing sub-arrays #4 and #1.

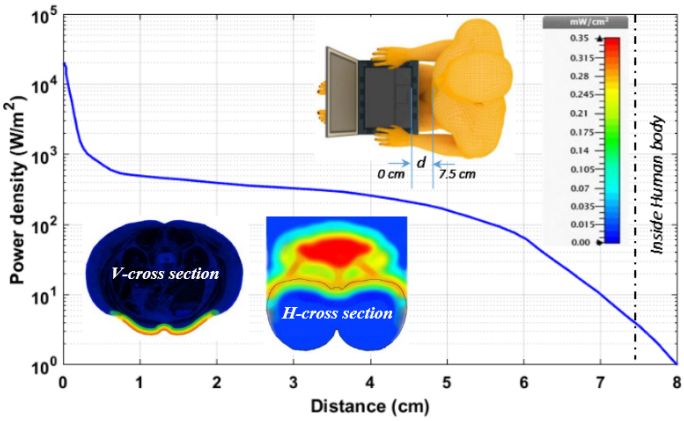


**Figure 16.** Power density versus distance with inserted vertical and horizontal cross section power distribution.

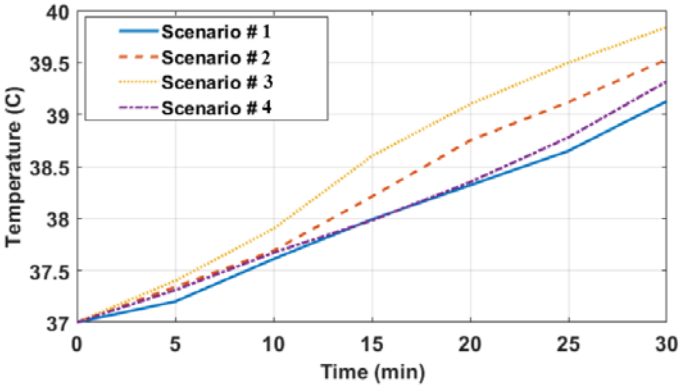


**Figure 17.** The maximum exposure temperature value versus exposure time.

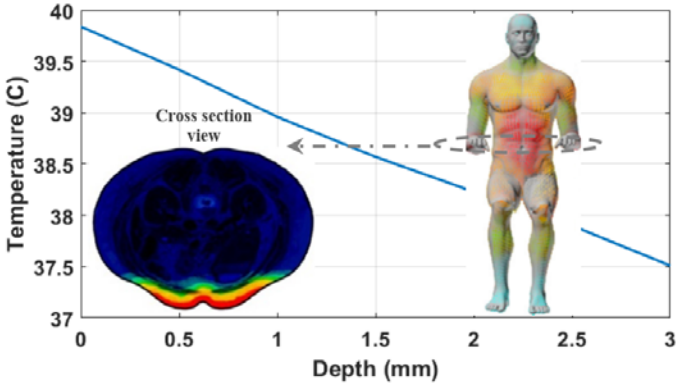


**Figure 18.** The exposure temperature versus penetration depth for scenario #3.

The figure shows the degradation of the power density (PD) value as the distance increases, whereas the PD is found to be 3.5 W/m$^2$ at the surface of the human's belly which is less than the standard threshold (10 W/m$^2$) by 65% and decreased to 1 W/m$^2$ after 0.5 mm only. The inserted figures in Fig. 16 show the distribution of power absorption in the tissues through the vertical and horizontal cut planes, respectively. It is clear that the PD is approximately 0 after only 3 mm from the abdominal surface.

Due to the more direct relationship between temperature and safety calculations, estimating the temperature value may be preferable to SAR and/or PD calculations. Therefore, a transient solver

with input power of 125 mW proceeds for different scenarios to calculate the maximum temperature rise with time as shown in Fig. 17. As it is expected, scenario #3 is the worst one with an increase in temperature exceeding 2.8°C after 30 minutes. Therefore, it was very important to investigate the temperature distribution for this case on an axial plane passing through mid-abdominal after exposure to radiation for 30 minutes. Fig. 18 shows the degradation in temperature with the penetration depth, whereas the temperature is decreased to 37.5° after 3 mm. The inset figure in Fig. 18 shows the cross-section cut in the human body in the area of beam penetration to see how deep the exposure temperature inside the human body. It is clear that the RF exposure is entirely absorbed in the human body epidermis and dermis.

In order to minimize the RF exposure to the human body, many techniques can be considered such as adding an appropriate RF shield [40], designing different metamaterials [41], or reducing near-field radiation [42] by adding it into the objective function of the beamforming optimization problem. Finally, the average radiated power from the communication device can be controlled to reduce the RF exposure [43].

## 4. CONCLUSION

In this paper, CP phased sub-array antennas have been presented for mm-wave 5G laptop devices. Firstly, a single-feed CP antenna array element is designed to resonate at 28 GHz with high gain value and radiation efficiency of 7.93 dB and 86%, respectively. Then, the performance of sub-arrays antennas to steer the beam-patterns in different directions has been introduced in the existence of whole-body human model. Furthermore, the radiation effects of the sub-arrays embedded into 5G laptop have been investigated by calculating the SAR and temperature rise. The obtained results demonstrate the superior performance of the designed sub-arrays in terms of radiation and beamforming characteristics. The lowest realized gain value for different scenarios is found to be 16.26 dBi with radiation and coverage efficiencies of 80% and 74.13%, respectively. Regarding the RF exposure, the results show that the peak SAR value is less than 1.52 W/kg, whereas the maximum exposure temperature is less than 2.8°C after 30 minuted and decreases to 0.5°C after only 3 mm which reflects the possibility of safe use.

## ACKNOWLEDGMENT

The authors would like to express their gratitude to the National Telecommunication Regulatory Authority (NTRA), Ministry of Communication and Information Technology in Egypt for their support. Further, they would like to thank the Deanship of Scientific Research at Umm Al-Qura University for partially supporting this work by grant code 19-COM-1-01-0015.

## REFERENCES

1. Sarraf, S., "5G will significantly impact the tech industry," *American Scientific Research Journal for Engineering, Technology, and Sciences*, Vol. 55, No. 1, 75–82, May 2019.
2. Accessed: Jan. 2021. [Online]. Available: https://www.delltech-nologies.com/en-us/latitude/latitude-9510-coming-soon.htm.
3. Accessed: Jan. 2021. [Online]. Available: https://www8.hp.com/us/en/laptops/2-in-1s/elite-dragonfly-convertible.html.
4. Accessed: Jan. 2021. [Online]. Available: https://www.lenovo.com/gb/en/laptops/yoga/yoga-c-series/Lenovo-Yoga-5G-p/88YGC801370.
5. Accessed: Jan. 2021. [Online]. Available: https://news.itu.int/wrc-19-agrees-to-identify-new-frequency-bands-for-5g/.
6. Naqvi, A. H. and S. Lim, "Review of recent phased arrays for millimeter-wave wireless communication," *MDPI Sensors (Basel)*, Vol. 18, No. 10, 1–31, Oct. 2018.
7. Mahmoud, K. R. and A. M. Montaser, "Optimised $4 \times 4$ millimetre-wave antenna array with DGS using hybrid ECFO-NM algorithm for 5G mobile networks," *IET Microw., Antennas Propag.*, Vol. 11, No. 11, 1516–1523, Aug. 2017.

8. Mahmoud, K. R. and A. M. Montaser, "Design of compact mm-wave tunable filtenna using capacitor loaded trapezoid slots in ground plane for 5G router applications," *IEEE Access*, Vol. 8, 27715–27723, 2020.
9. Balanis, C. A., *Antenna Theory: Analysis and Design*, John Wiley & Sons, 2016.
10. Hesari, S. S. and J. Bornemann, "Wideband circularly polarized substrate integrated waveguide endfire antenna system with high gain," *IEEE Antennas Wireless Propag. Lett.*, Vol. 16, 2262–2265, 2017.
11. Hussain, N., M.-J. Jeong, J. Park, and N. Kim, "A broadband circularly polarized Fabry Perot resonant antenna using a single-layered PRS for 5G MIMO applications," *IEEE Access*, Vol. 7, 42897–42907, 2019.
12. Lin, Q. W., H. Wong, X. Y. Zhang, and H. W. Lai, "Printed meandering probe-fed circularly polarized patch antenna with wide bandwidth," *IEEE Antennas Wireless Propag. Lett.*, Vol. 13, 654–657, 2014.
13. Hussain, N., M. Jeong, A. Abbas, T. Kim, and N. Kim, "A metasurface-based low-profile wideband circularly polarized patch antenna for 5G millimeter-wave systems," *IEEE Access*, Vol. 8, 22127–22135, 2020.
14. Mahmoud, K. R. and A. M. Montaser, "Synthesis of multi-polarised upside conical frustum array antenna for 5G mm-wave base station at 28/38 GHz," *IET Microwave Antennas Propag.*, Vol. 12, No. 9, 1559–1569, Jul. 2018.
15. Accessed: Jan. 2021. [Online]. Available: https://www.micro-wavejournal.com/articles/27830-ibm-and-ericsson-announce-5g-mmwave-phase-array-antenna-module.
16. Mahmoud, K. R. and A. M. Montaser, "Performance of tri-band multi polarized array antenna for 5G mobile base station adopting polarization and directivity control," *IEEE Access*, Vol. 6, 8682–8694, 2018.
17. Xu, B., et al., "Power density measurements at 15 GHz for RF EMF compliance assessments of 5G user equipment," *IEEE Trans. Antennas Propag.*, Vol. 65, No. 12, 6584–6595, Dec. 2017.
18. Colombi, D., B. Thors, C. Törnevik, and Q. Balzano, "RF energy absorption by biological tissues in close proximity to millimeter-wave 5G wireless equipment," *IEEE Access*, Vol. 6, 4974–4981, 2018.
19. Xu, B., M. Gustafsson, S. Shi, K. Zhao, Z. Ying, and S. He, "Radio frequency exposure compliance of multiple antennas for cellular equipment based on semidefinite relaxation," *IEEE Trans. Electromagn. Compat.*, Vol. 61, No. 2, 327–336, Apr. 2019.
20. Colombi, D., B. Thors, and C. Törnevik, "Implications of EMF exposure limits on output power levels for 5G devices above 6 GHz," *IEEE Antennas Wireless Propag. Lett.*, Vol. 14, 1247–1249, 2015.
21. Zhao, K., Z. Ying, and S. He, "EMF exposure study concerning mmWave phased array in mobile devices for 5G communication," *IEEE Antennas Wireless Propag. Lett.*, Vol. 15, 1132–1135, 2016.
22. He, W., B. Xu, M. Gustafsson, Z. Ying, and S. He, "RF compliance study of temperature elevation in human head model around 28 GHz for 5G user equipment application: Simulation analysis," *IEEE Access*, Vol. 6, 830–838, 2018.
23. Thors, B., D. Colombi, Z. Ying, T. Bolin, and C. Törnevik, "Exposure to RF EMF from array antennas in 5G mobile communication equipment," *IEEE Access*, Vol. 4, 7469–7478, 2016.
24. Mahmoud, K. R. and A. M. Montaser, "Design of dual-band circularly polarised array antenna package for 5G mobile terminals with beam-steering capabilities," *IET Microwave Antennas Propag.*, Vol. 12, No. 1, 29–39, 2018.
25. Hamed, T. and M. Maqsood, "SAR calculation & temperature response of human body exposure to electromagnetic radiations at 28, 40 and 60 GHz mmWave frequencies," *Progress In Electromagnetics Research M*, Vol. 73, 47–59, 2018.
26. Zhadobov, M., N. Chahat, R. Sauleau, C. L. Quement, and Y. L. Drean, "Millimeter-wave interactions with the human body: State of knowledge and recent advances," *International Journal of Microwave and Wireless Technologies*, Vol. 3, No. 2, 237–247, 2011.

27. International Commission on Non-Ionizing Radiation Protection, "Guidelines for limiting exposure to electromagnetic fields (100 kHz to 300 GHz)," *Health Physics*, Vol. 118, No. 5, 483–524, 2020.
28. IEEE Standards Coordinating Committee, 28, "IEEE standard for safety levels with respect to human exposure to electric, magnetic, and electromagnetic fields, 0 Hz to 300 GHz," IEEE C95.1TM-(2019), 1–310, 2019.
29. Wu, T., T. S. Rappaport, and C. M. Collins, "Safe for generations to come: Considerations of safety for millimeter waves in wireless communications," *IEEE Microwave Mag.*, Vol. 16, No. 2, 65–84, Mar. 2015.
30. Shrivastava, P. and T. R. Rao, "Investigations of SAR distributions and temperature elevation on human body at 60 GHz with corrugated antipodal linear tapered slot antenna," *Progress In Electromagnetics Research M*, Vol. 59, 111–121, 2017.
31. Zhang, W.-X., J. Wang, R. Tao, H.-L. Peng, G. Guo, and J.-F. Mao, "A simplified model of specific absorption rate calculation for laptop mounted equipment in near proximity to human torso," *Journal of Electromagnetic Waves and Applications*, Vol. 26, 757–769, 2012.
32. Ahmed, M. I., M. F. Ahmed, and A. H. A. Shaalan, "SAR calculations of novel textile dual-layer UWB lotus antenna for astronauts spacesuit," *Progress In Electromagnetics Research C*, Vol. 82, 135–144, 2018.
33. Montaser, A. M., K. Mahmoud, and H. A. Elmikati, "An interaction study between PIFAs handset antenna and a human hand-head in personal communications," *Progress In Electromagnetics Research B*, Vol. 37, 21–42, 2012.
34. Kong, L.-Y., J. Wang, and W.-Y. Yin, "A novel dielectric conformal FDTD method for computing SAR distribution of the human body in a metallic cabin illuminated by an intentional electromagnetic pulse (Iemp)," *Progress In Electromagnetics Research*, Vol. 126, 355–373, 2012.
35. Sabbah, A. I., N. I. Dib, and M. A. Al-Nimr, "Evaluation of specific absorption rate and temperature elevation in a multi-layered human head model exposed to radio frequency radiation using the finite difference time domain method," *IET Microwave Antennas Propag.*, Vol. 5, No. 9, 1073–1080, 2011.
36. Azim, R., M. T. Islam, and N. Misran, "Ground modified double-sided printed compact UWB antenna," *Electronics Letters*, Vol. 47, No. 1, 9–11, 2011.
37. Nguyen, N. L., "Gain enhancement in MIMO antennas using defected ground structure," *Progress In Electromagnetics Research M*, Vol. 87, 127–136, 2019.
38. Accessed: Oct. 2019. [Online]. Available: https://itis.swiss/virtual-population/virtual-population/overview/.
39. Accessed: Dec. 2019. [Online]. Available: https://www.3ds.com/products-services/simulia/products/cst-studio-suite/.
40. Stephen, J. P. and D. J. Hemanth, "An investigation on specific absorption rate reduction materials with human tissue cube for biomedical applications," *International Journal of RF and Microwave Computer-Aided Engineering*, Vol. 29, No. 12, 1–19, 2019.
41. Islam, M. T., M. R. I. Faruque, and N. Misran, "Reduction of specific absorption rate (SAR) in the human head with ferrite material and metamaterial," *Progress In Electromagnetics Research C*, Vol. 9, 47–58, 2009.
42. Montgomery, M. T., M. C. Frank, P. A. Tornatta, Jr., M. W. Kishler, and L. Chen, "Methods for reducing near-field radiation and specific absorption rate (SAR) values in communications devices," U.S. Patent 8,344,956, issued January 1, 2013.
43. Nevermann, P., "System and method for reducing SAR values," U.S. Patent 7,146,139, issued December 5, 2006.